Signal-to-Signal-to-Noise-Ratio of Full-Field Fourier-Domain Optical Coherence Tomography: Experiment

P. Blazkiewicz[1], P. M. Gourlay[1], J. R. Tucker[2], M. Gujrathi[2], A. Rakic[2] and A. Zvyagin[1,2]
[1]Centre for Biophotonics and Laser Centre for Biophotonics and Laser Science, Physics, University of Queensland, Brisbane, QLD, Australia, 4072.
[2]School of Information Technology and Electrical Engineering, University of Queensland, Brisbane, QLD, Australia, 4072

ABSTRACT

We report a new approach in optical coherence tomography (OCT) termed full-field Fourier-domain OCT (3F-OCT). A three-dimensional image of a sample is obtained by digital reconstruction of a three-dimensional data cube, acquired using a Fourier holography recording system illuminated with a swept-source. This paper presents theoretical and experimental study of the signal-to-noise ratio of the full-field approach versus serial image acquisition approach, represented by 3F-OCT and "flying-spot" OCT systems, respectively.

Keywords: optical coherence tomography, coherence-domain imaging, holography

1. INTRODUCTION

Optical coherence tomography (OCT) is playing an important role in the advancement of optical imaging in biomedicine by way of its ability to generate high-resolution images of unprecedented quality *in vivo* within turbid media at millimeter-scale depths [1,2]. In its conventional form, termed time-domain OCT (TD-OCT), the reference arm of a Michelson interferometer is scanned to obtain a one-dimensional reflectivity profile of the sample in depth, i.e. along the optical axis (A-scan) [3]. An alternative approach to obtain an A-scan is based on processing the spectral content of the heterodyne signal at the output of the stationary Michelson interferometer via discrete Fourier transform (DFT). This concept implementation has been recently demonstrated as spectral-domain OCT (SD-OCT) [4,5] and swept-source OCT (SS-OCT) [6]. It has been also demonstrated that the signal-to-noise ratio (SNR) of this new parallel data acquisition approach is improved as compared with that of TD-OCT, which represents serial data acquisition approach [4].

In order to obtain a two-dimensional (2D), or three-dimensional (3D) image of the sample, the probe beam is scanned across the sample in a lateral plane in addition to A-scans taken at each lateral point. This lateral scanning is usually realized by means of a "flying-spot" optical circuit containing mechanical scanners that are expensive and cumbersome to operate. Importantly, SNR of flying-spot configuration is not optimised, as compared to that achievable with full-field configurations.

We report a full-field system, called full-field Fourier-domain OCT (3F-OCT), which has the potential to overcome these limitations [7]. In 3F-OCT, the optical field disturbance due to the sample is full-field-projected onto a 2D digital sensor, where it is superimposed coherently with a plane reference wave, as shown in Figure 1.

Coherence Domain Optical Methods and Optical Coherence Tomography in Biomedicine IX, edited by Valery V. Tuchin, Joseph A. Izatt, James G. Fujimoto, Proc. of SPIE Vol. 5690 (SPIE, Bellingham, WA, 2005) · 1605-7422/05/$15 · doi: 10.1117/12.592284

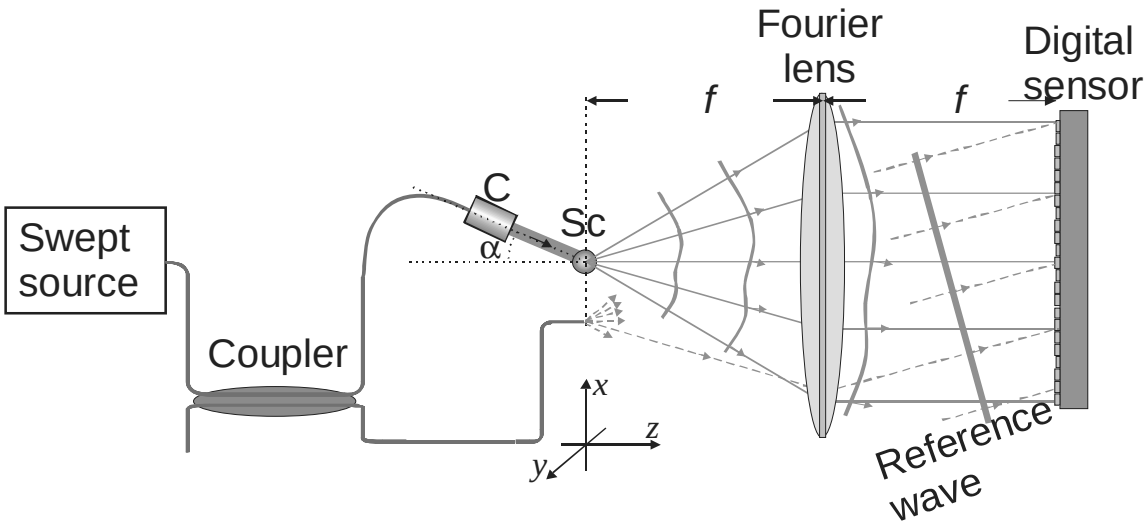

Figure 1: Schematic diagram of 3F-OCT, C, collimator; Sc, scatterer; α – angle of incidence.

In 3F-OCT we use a holographic interferometer instead of the Michelson interferometer typically used for "flying spot" OCT configurations. Here for simplicity we describe 3F-OCT in the transmission mode (extendable to reflection mode). Our optical source is launched into a fiber-optic coupler which splits the light into the sample and reference arms. A sample is located at the front focal plane of a Fourier lens, this is shown as a point like scatterer in Figure1. The scatterer is illuminated at an angle α, by a collimated beam from the sample arm optical fiber (single-mode). The collimated beam is scattered by the sample, this scattered light is collected by the lens and directed towards a 2D CCD array. A reference beam is created by placing the distal tip of the reference optical fiber (single-mode) in the focal plane near the sample. Light from the reference fiber is collimated at a small angle by the lens and interferes with light scattered from the sample arm. The hologram produced by the interference of the sample and reference beams is digitally recorded using a 2D CCD array. Each hologram measured at the digital sensor is directly related to the 2D Fourier transform of the scattered optical field emanating from the sample. To obtain axial imaging along the z-axis (A-scan), we use a swept source and record holograms for a set of wavenumbers spanning our sweep range. Collating the set of holograms we form a 3D-data cube, which is the 3D-Fourier transform of our sampling region. Our sample image is reconstructed by performing a 3D Fourier transform on the data-cube.

Several full-field OCT systems have been previously reported [8,9,10]. A 3D full-field system based on holography has been first described by Wolf *et al.* [11], and subsequently demonstrated by others [12]. However, the SNR analysis of this approach has not been addressed. In this paper, we present theoretical and experimental study of signal-to-noise ratio of 3F-OCT. The SNR of the full-field approach (3F-OCT) versus serial image acquisition approach ("flying-spot" OCT systems) will be analyzed theoretically and verified experimentally. In order to establish grounds for this analysis, in the next Section, we will present initial results of the imaging performance of 3F-OCT.

2. IMAGING OF A POINT SOURCE

We have implemented our 3F-OCT system prototype, in transmission mode as described above and shown in Figure 1. To create a point-like scatterer, the sample-arm fiber tip was placed at the focal plane of the Fourier lens, at a tilt angle of $\alpha = 0$ and without a collimator. Our swept-source was a cw stepper-motor-driven wavelength-tunable titanium-sapphire laser (Mira 900, Coherent). Our holograms were acquired using a 1040×1392 CCD camera (Samba EZ-140 monochrome, Sensovation). A set of 80 Fourier holograms was acquired at discrete wavenumbers to form a three-dimensional data cube. A DFT was used to reconstruct the image of our optical fiber tip [7].

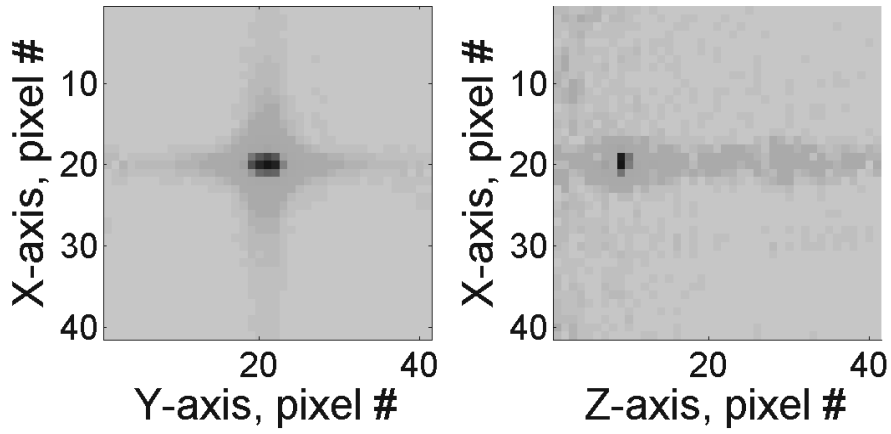

Figure 2: Two sections through a 3D-image of the scatterer: *x*-*y* plane, lateral cross-section (left panel); and *x*-*z* plane, axial cross-section (right panel). *x*, *y*, and *z* - dimensions of the pixel are 8, 6, and 6.7 μm, respectively. The swept-source wavelength range was 100 nm, centered at 820 nm; sweep time, 10 s. NA of the fiber, 0.12; f = 100 mm.

The cross-sectional reconstructions of our data-cube are shown in Figure2. The left panel is the lateral cross-section looking directly onto the fiber tip, and the right panel is the axial cross-section along the optical fiber axis. Convergence to a single-peak image is clearly observable on both panels, indicating the reconstruction of a point source at the distal end of the sample optical fiber. These images, although noisy due to the quality of our swept-source, clearly demonstrate the technique fidelity of mapping of a single scatterer in three-dimensional space.

3. SIGNAL-TO-NOISE RATIO ANALYSIS

The fundamental difference between flying-spot and full-field illumination configurations is encapsulated by the data acquisition mode in the lateral, i.e. *x*-*y*, plane. Therefore, when comparing these two techniques in terms of their SNR, it is sufficient to consider monochromatic illumination. The use of a swept-source to optimize the OCT SNR in the axial direction (*z*-axis) is considered elsewhere [13]. To further simplify the analysis, we consider the OCT signal acquisition in a single lateral dimension, e.g. *x* [see Figure 1].

In the flying-spot configuration, the number of photoelectrons received by a single-pixel detector integrated over exposure time, τ_{FS} is given by

$$\phi_{FS} = \rho\tau_{FS}\left(P_r + \sigma_{sc}I_0 + 2\sqrt{P_r I_0 \sigma_{sc}}\right), \qquad (1)$$

where $\rho = \eta/(h\nu)$ is the detector responsivity, η is the detector quantum efficiency, $h\nu$ is the energy of a photon; P_r denotes power of the light source in the reference arm, I_0 is irradiance in the sample arm (power per unit area) and σ_{sc} denotes the scattering cross-section of a point-like scatterer. We assume that all scattered photons are detected and the NA of the collection optics is equal for both configurations. A zero optical path difference of the sample and reference arms is also assumed. The signal from the scatterer is given by the third term in the brackets. The dominant shot noise is due to the reference arm power [first term in the brackets of Eq. (1)] and is expressed in terms of its standard deviation:

$$\left\langle \phi^2_{noise,FS} \right\rangle = \rho\tau_{FS}P_r, \qquad (2)$$

In 3F-OCT, the photoelectron signal detected during the exposure time, τ_{3F} is expressed as

$$\phi_{3F} = \rho\tau_{3F}\left(P_r + \sigma_{sc}I_0 + 2\sqrt{P_r I_0 \sigma_{sc}}\cos[\kappa_n x_s]\right)/N\,, \tag{3}$$

where $\kappa_n = (k_0 L_{CCD}/f)\cdot(n/N)$, $0 \le n \le N-1$; L_{CCD} is the lateral dimension of the digital sensor, k_0 is a wavenumber of the source, *f* is the focal length of the lens, *n* is the index of the detector element and x_s is the *x*-coordinate of the scatterer. A factor of $1/N$ is introduced as the reference and scattered power is uniformly distributed across *N* elements of the CCD. The sampled 3F-OCT signal is given by the third term in the brackets, Eq. (3), whereas the sampled shot noise is expressed as:

$$\left\langle \phi^2_{noise,3F} \right\rangle = \rho\tau_{3F}\, P_r/N\,. \tag{4}$$

In order to reconstruct an image of the scatterer, a DFT of the signal is performed [14]. Since the signal is a harmonic function, its power spectrum represents two single-peak sidelobes of amplitude $2\rho^2\tau_{3F}^2 P_r I_0 \sigma_{sc}$, of which only one sidelobe represents the sample reconstruction. Using Eq. (4), DFT of the noise is given by

$$\Im\left[\left\langle \phi^2_{noise,3F} \right\rangle\right] = \rho\tau_{3F} P_r\,, \tag{5}$$

where $\Im$ denotes a DFT operator. Note the incoherent summation of uncorrelated components of noise resulting to this expression. Comparison of the 3F-OCT and flying-spot configurations in terms of their respective SNR yields:

$$\frac{SNR_{3F}}{SNR_{FS}} = \frac{1}{2}\frac{\tau_{3F}}{\tau_{FS}}\,. \tag{6}$$

We point out that the SNR ratio can be also expressed in terms of detector bandwidths, *BW*, in case of a linear detector array, using $BW = 1/(2\tau)$.

The lateral resolution of 3F-OCT is $\delta x = \pi f/(k_0 L_{CCD})$, and the total reconstructed lateral field size is $(N/2)\delta x$. Thus, τ_{FS} must be $N/2$ times shorter than τ_{3F} to maintain the same frame rate when acquiring only $N/2$ lateral pixels. From analysis of Eq. (6), it is obvious that SNR of 3F-OCT is *N*/4 times greater than that of the flying-spot OCT. Note that we have assumed equal irradiance of the sample in both cases. If we assume equal illumination power, the SNR of 3F-OCT is half that achieved by the flying-spot OCT configuration. It is important to note that there is a broad class of OCT applications, where comparison of SNR in terms of equal irradiance is meaningful, since amount of irradiance is limited by the laser safety standards. In particular, it relates to imaging of the eye using OCT. In the next Section, we will show that the amount of power permissible at the live human eye is much greater in case of full-field illumination, represented by 3F-OCT, as compared to serial illumination, represented by flying-spot OCT.

4. MAXIMUM PERMISSIBLE OCULAR EXPOSURE

Laser safety standards limit the irradiance at the cornea, which limits the amount of power that can be launched safely into the eye. Using with full-field configurations it is possible to launch more input power for applications where the irradiance at the cornea is limited.

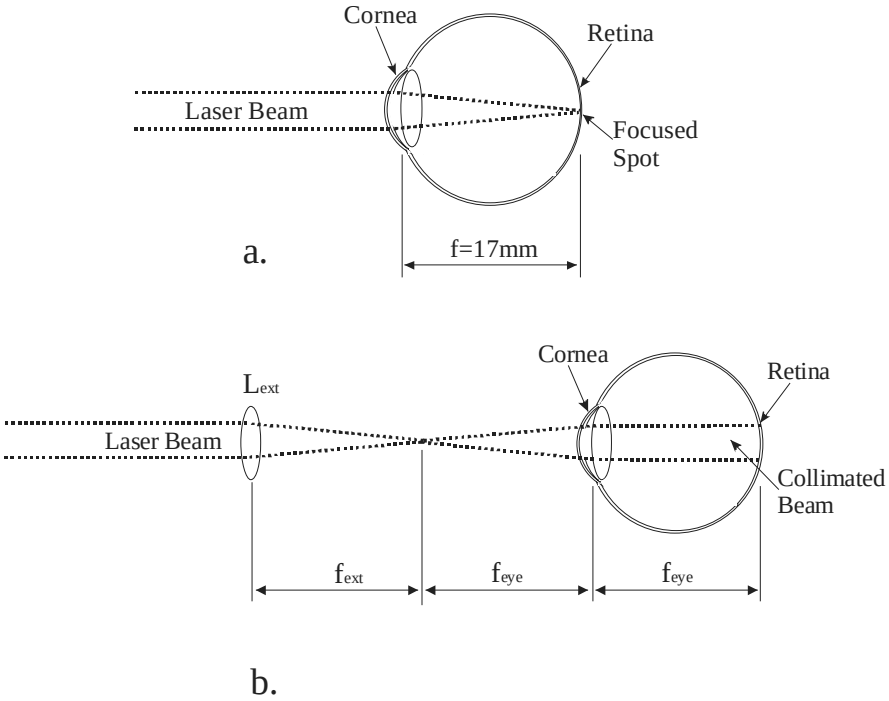

Figure 3: (a) Illumination of retina using flying spot OCT, (b) Illumination of eye using 3F-OCT.

A simplified diagram of illumination of the retina using flying-spot OCT and 3F-OCT, are shown in Figs. 3(a) and 3(b), respectively. In the flying spot case there is an increase in irradiance from the cornea to the retina, as the incident light is tightly focused. However, for the full-field case there is no change in irradiance from the cornea to the retina.

In the flying spot mode, the focused spot size is typically 25 μm in diameter. Assuming uniform illumination across a fully dilated pupil of diameter 7 mm, the increase in irradiance from the pupil to the retina is ~78400 times. This imposes severe restrictions on the amount of power that can be launched into the eye when using flying-spot mode for the OCT clinical applications. For exposure times of 10 seconds, the average MPE at 800nm is calculated to be 1.60 mW/cm^2 at the cornea, which allows 616 μW to be launched into the fully dilated eye [15]. Since the irradiance increases by a factor of 78400 at the retina, the irradiance at the retina is actually 125 W/cm^2.

In the full-field illumination mode, an external lens, L_{ext} of the focal length f_{ext}, is used to ensure that the beam incident on the retina is collimated [see Figure 3(b)]. In this configuration, the angle subtended by the illuminated region on the retina from the lens is 412 mrad. For exposure times of 10 seconds, the average power (MPE) is calculated to be 1.82 W/cm^2. Since there is no change in irradiance from the cornea to the retina, there is still only 1.82 W/cm^2 at the retina for the full-field configuration. Thus the irradiance at the retina is 69 times less than for the flying spot configuration. However, using this limiting irradiance at the cornea we calculate that 700mW can be launched into the fully dilated eye for the full-field configuration [15]. This may seem to be an extraordinary claim, if one does not realize that the irradiance at the retina is 69 times lower than the flying spot retinal irradiance.

It may be argued that the MPE is actually greater in case of flying-spot illumination, since individual regions on the retina are illuminated for a short time. It is plausible to model this case as pulsed laser illumination of a focused spot on the retina. The laser pulse width is given by the flying-spot dwell time and the pulse repetition rate is simply the frame rate of the OCT system. We use the reported video-frame-rate SD-OCT system (29 frames/second), and flying-spot dwell time of 34.1 μs to calculate the repetitive pulse limit MPE[16]. Using these values, the peak irradiance MPE in the repetitive pulse limit is 9.0 mW/cm^2 measured at the pupil, which allows 3.50 mW to be launched into the fully dilated eye[15].

Thus, full-field illumination OCT configurations, including 3F-OCT, allow more optical power to be safely launched into a fully dilated pupil, compared to flying-spot OCT configurations. This gives full-field illumination configurations an SNR advantage over flying spot configurations. Using Eq. (6) presented in Section 3, the attainable improvement of 3F-OCT SNR is evaluated to be a factor of 100 greater than that of the flying-spot OCT using the repetitive pulse limit MPE (can be 568 times greater when using the average power limit MPE).

However, there is an issue of using stable and accurate alignment in the full-field configuration. If the patient moves the beam will no longer be collimated and the MPE may be exceeded, thus adequate restraint of the patient will be required. In addition, the current laser standards may not be adequate for extended source viewing when the angle subtended by the illuminated spot is very large. It may be necessary to produce new standards that address the issue of full-field illumination of the eye.

5. EXPERIMENTAL COMPARISON OF SNR FOR 3F-OCT VERSUS FLYING-SPOT OCT

The SNR of flying-spot and full-field OCT configurations were tested experimentally using a hybrid time-domain/3F-OCT system with equal irradiance in both cases. Our hybrid time-domain/3F-OCT system is analogous to the hybrid TD/spectral-domain OCT reported by de Boer *et al.* [5]. The system demonstrated by de Boer *et al.* experimentally compared serial and parallel OCT configurations for axial depth scans using a broadband source. Whereas, our hybrid system compares serial and parallel OCT configurations for lateral scans using a monochromatic source.

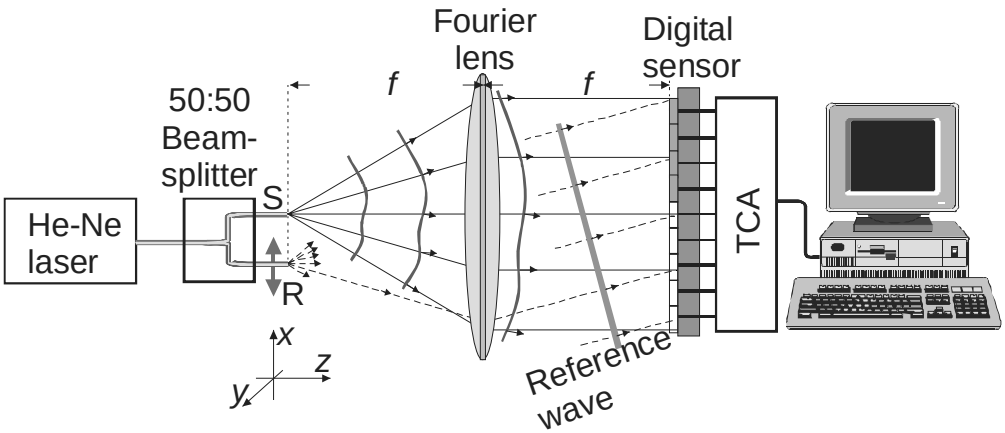

Figure 4: Schematic diagram of the hybrid TD/3F-OCT experimental setup. S, sample fiber; R, scanning reference fiber; TCA, trans-conductance amplifier. In the digital sensor, shaded boxes represent off-axis detectors employed in the experiment. (Not to scale).

The experimental setup of the hybrid TD/3F-OCT system is presented in Figure 4. The optical circuit represents a Fourier holography system with one important difference: the reference fiber is not stationary. The output beam from a He-Ne laser of a wavelength of $\lambda = 632.8$ nm is equally split (50:50) between the fiber-optic sample and reference arms, whose distal ends are situated at the front focal plane of a Fourier lens with focal length, f = 100 mm. The fibers are closely separated in the vertical y-direction (< 1 mm) to allow the horizontal translation of the reference fiber, i.e.

along the *x*-axis (see Figure 2), with a constant velocity of $v = 300\,\mu\mathrm{m/s}$. The sample fiber is placed on-axis and represents a point-like source. The reference fiber is initially placed at a distance x_s off-axis. It produces a plane reference wave that is incident at an angle on the detector array placed at the back focal plane of the Fourier lens. The reference and sample optical fields interfere across the detector array to produce an interference pattern. Translation of the reference fiber causes variation of the fringe pattern in time. This results in the generation of a time-varying signal at each detector element, i_d which, is found by integrating the detector photoresponse over the detector element width, *d* (*d* = 0.82 mm):

$$i_d = 2P_0\rho q\left[1 + \mathrm{sinc}\left[(\omega/v)x_s - \omega t\right]\cos(2n\omega t)\right], \qquad (7)$$

P_0 is the incident power in one arm, *q* is an elementary charge, $\omega = \pi v d/(\lambda f)$ is the angular frequency of the signal, and *n* is the index of the detector element, where *n* = 0 denotes the on-axis detector element.

In general, the translation of a single fiber produces frequency chirp. It turns out to be insignificant, as the signal is recorded in the vicinity of the central peak of the sinc-function, and is omitted from Eq. (7). Examination of Eq. (7) shows that the a.c. signal represents a sinc-function envelope peaking at $t = x_s/v$, modulated by a constant carrier frequency. The carrier frequency is proportional to the index of the detector element. Since it was desirable to attain a relatively high carrier frequency, the detector elements were placed several millimeters off-axis. In our experiment, the envelope width was measured to be 3.89 Hz, and the carrier frequency varied from 23 to 73 Hz at a discrete frequency step of 4.83 Hz. The small mismatch between the envelope width and a discrete frequency step was due to a gap between the detector elements of 0.2 mm. A horizontal slit (*x*-axis) was placed in front of the detector array to eliminate a signal acquisition artefact due to the finite vertical separation of the fibers (not shown in Figure 4).

In our experiment, the time-varying signals from ten adjacent detectors were individually recorded, and subsequently processed in software. We employed two filtering schemes pertinent to the flying-spot and full-field OCT configuration. To synthesize the flying-spot signal, the ten channel amplitude spectrums were summed up following broad bandpass filtering using a 2nd-order Butterworth filter (*BW* = 50.0 Hz). The processed signal is shown in Figure 5 (blue, dotted curve). To synthesize the full-field signal, each signal was narrow band-pass filtered (*BW* = 5.0 Hz), and these frequency responses were summed in the Fourier-domain. The result is shown in Figure 5 (red, solid curve). The noise power in the narrow band-passed case was reduced by a factor of 9.74, which agrees well with the calculated value of the ratio of the full-field to flying-spot SNR's of BW_{3F}/BW_{FS} = 10.0 [c.f. Eq. (6) corrected for the factor of ½ due to the additional DFT of the flying-spot signal]. An overall SNR improvement was estimated to be 7.55 taking into account the signal reduction factor of 1.29 due to the filtering.

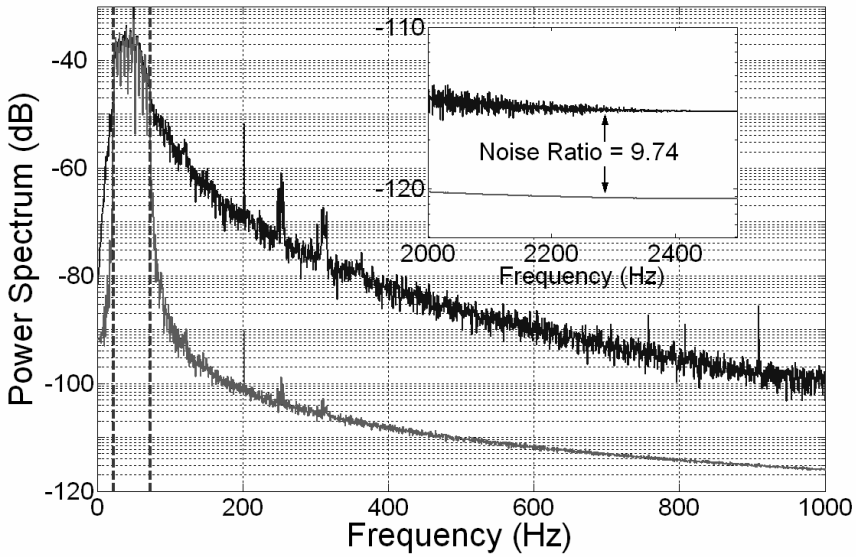

Figure 5: Logarithmic plot of two signals pertinent to flying-spot (upper curve) and full-field (lower curve) OCT acquired from ten detectors using experimental setup of Figure 4. See details in text.

6. DISCUSSION

Our 3F-OCT technique is a method for optimizing SNR performance under shot-noise limited conditions of the detection system. We have demonstrated that that SNR of 3F-OCT is optimal compared to flying-spot OCT, when the illumination irradiance is limited in the sample arm. Such comparisons are useful in the context of biological imaging, as the illumination irradiance of samples *in vivo* is limited by laser safety standards. In particular, there is a large increase in available launch power into the eye, if there is no focusing of the input power onto the retina. Also in 3F-OCT, image acquisition in the axial dimension takes place in spectral domain, as opposed to image acquisition in time-domain demonstrated in the other reported full-field OCT systems [8,9,10]. Theoretically, the SNR of 3F-OCT is expected to be larger by a factor of $M/2$ (M – number of sampled wavenumbers) than the SNR of the time-domain full-field OCT. Our analysis presented above shows that there is scope to improve SNR of SD-OCT and SS-OCT systems by employing full-field image acquisition in place of lateral scanning of the focused spot (flying-spot mode), when the maximum permissible exposure represents a constrain on the amount of power in the sample arm.

Our full-field strategy to optimize SNR of SD(SS)-OCT systems can be called full-field Fourier-domain OCT, wherein 3F-OCT represents one particular implementation of this strategy. Alternatively, the full-field Fourier-domain OCT can be realized using direct full-field imaging in the lateral plane (*on face*) instead of Fourier holographic imaging, as addressed in this paper. This technique capable of acquiring two-dimensional images in parallel of improved SNR has been reported by Vakhtin *et al*. [17]. However, to our best knowledge, the full-field Fourier-domain OCT featuring a swept-source, capable of acquisition of 3D-images in parallel, has not been reported.

In the above argument we have shown that the SNR of 3F-OCT is improved under shot-noise limited conditions. However, other sources of noise can be quite detrimental, for example in Section 2 our imaging of a point source was affected by the wavelength tuning stability of our Ti: sapphire laser. We found our laser suffered from mode-hops that in turn lead to phase jumps, which were detrimental to our signal acquisition. These phase jumps were our dominant source of noise creating a depth dependent phase-error. In addition, it should be mentioned that full-field spectral-domain OCT is envisaged to be prone to a cross-talk imaging artefact, which will also cause the SNR degradation [18]. The effect of the cross-talk on 3F-OCT warrants separate study.

However, our Fourier holography approach of recording full-field OCT data does confers several advantages [19]. Among those, due to the digital nature of the recorded data, it allows flexible adaptable control and filtering of the angular scatter signal. This has been demonstrated by Boustany *et al.* called optical scatter imaging [18]. The optical scatter imaging technique has been reported to be sensitive to minute variation of small-size cell constituents, which are undetectable using conventional microscopy. In addition, the Fourier holographic method of recording data is expected to have an advantage of improved contrast, as applied to imaging of small-size scatterers due to efficient rejection of low-frequency optical scatter components stemming from large-scale structures [19].

7. CONCLUSION

In conclusion, we have reported a full-field OCT configuration that represents a combination of swept-source OCT and digital Fourier holography. The full-field Fourier-domain OCT imaging capability has been demonstrated by imaging a point-like scatterer. Our comparative SNR analysis of conventional flying-spot versus full-field OCT configurations has revealed an advantage of 3F-OCT, when the permissible irradiance is limited, as in ophthalmology. The experimental study of SNR using a hybrid time-domain/3F-OCT system has confirmed our theoretical analysis.

ACKNOWLEDGEMENTS

The authors would like to thank A/Prof. Norman Heckenberg and Dr. Taras Plakhotnik for helpful discussions.

REFERENCES

1. D. Huang, E. A. Swanson, C. P. Lin, J. S. Schuman, W. G. Stinson, W. Chang, M. R. Hee, T. Flotte, K. Gregory, C. A. Puliafito, and J. G. Fujimoto, "Optical coherence tomography", Science, Vol. 254, (1991), pp.1178
2. Brett E. Bouma and Guillermo J. Tearney, "Handbook of Optical Coherence Tomography", (Marcel Dekker, Inc, NewYork, 2002) pp. 26
3. M. E. Brezinski and J. G. Fujimoto, IEEE Journal of Selected Topics in Quantum Electronics, Vol. 5, (1999), pp.1185
4. R. Leitgeb, C. K. Hitzenberger, and A. F. Fercher, 'Performance of fourier domain vs. time domain optical coherence tomography', Optics Express, Vol. 11, Issue 8, (2003), pp.889
5. J. F. de Boer, B. Cense, B. H. Park, M. C. Pierce, G. J. Tearney and B. E. Bouma, 'Improved signal-to-noise ratio in spectral-domain compared with time domain optical coherence tomography', Optics Letters, Vol. 28, (2003), pp.2067
6. Michael A. Choma, Marinko V. Sarunic, Changuei Yang, Joseph A. Izzat, "Sensitivity advantage of swept source and Fourier domain optical coherence tomography", Optics Express, Vol. 11, No. 18, (2003) pp. 2183
7. A. V. Zvyagin, "Fourier-Domain Optical Coherence Tomography: Optimization of Signal-to-Noise Ratio in Full Space", Optics Communications, Vol. 242, No. 1-3, (2004), pp. 97.
8. E. Beaurepaire, A. C. Boccara, M. Lebec, L. Blanchot & H. Saint-Jalmes, "Full-field Optical coherence microscopy", Optics Letters, Vol. 23, No. 4, (1998) pp.244
9. S. Bourquin, P. Seitz & R. P. Salathe, "Optical coherence topography based on a two-dimensional smart detector array", Optics Letters, Vol. 26, No. 8 (2001) pp.512
10. M. Laubscher, M. Ducros, B. Karamata, T. Lasser, R. Salathe, "Video-rate three-dimensional optical coherence tomography", Optics Express, Vol. 10, Issue 9, (2002), pp.429
11. E. Wolf, "Three dimensional structure determination of semi-transparent objects from holographic data", Optics Communications, Vol.1, No. 4, (1969) pp.153
12. E. Arons and D. Dilworth, "Analysis of Fourier synthesis holography for imaging through scattering materials", Applied Optics, Vol. 34, (1995), pp. 1841
13. S. H. Yun, G. J. Tearney, J. F. de Boer, N. Iftimia and B. E. Bouma, "High-speed spectral-domain optical coherence tomography at 1.3 μm wavelength", Optics Express, Vol. 11, No. 22, (2003), pp.2953
14. R. N. Bracewell, 'Fourier Transform and its Applications', Mc Graw-Hill, NewYork, (1978), Ch.18
15. American National Standards Institute, Safe Use of Lasers, ANSI Z136.1-2000, (Laser Institute of America, 2000)

16. N. A. Nassif, B. Cense, B. H. Park, M. C. Pierce, S. H. Yun, B. E. Bouma, G. J. Tearney, T. C. Chen and J. F. de Boer, 'In vivo high-resolution video-rate spectral-domain optical coherence tomography of the human ratina and optic nerve' , Optics Express, Vol. 12, No.3, (2004), pp. 367.
17. A. B. Vakhtin, K. A. Peterson, W. R. Wood, D. J. Kane, "Differential spectral interferometry: an imaging technique for biomedical applications", Optics Letters 28, (2003), pp.1332
18. Nada N. Boustany, Scot C. Kuo, Nitish V. Thakor , "Optical scatter imaging:subcellular morphometry in situ with Fourier filtering", Optics Letters, Vol. 26, No. 14, (2001) , pp.1063
19. S. A. Alexandrov, P. Meredith, T. J. McIntyre, A. V. Zvyagin, "Digital Fourier microscopy for selective imaging of biological tissue", submitted to International Journal of Imaging Systems Technology